

This is the accepted manuscript made available via CHORUS. The article has been published as:

Triplet fermions and Dirac fermions in borophene

Motohiko Ezawa

Phys. Rev. B **96**, 035425 — Published 20 July 2017

DOI: [10.1103/PhysRevB.96.035425](https://doi.org/10.1103/PhysRevB.96.035425)

Triplet Fermions and Dirac Fermions in Borophene

Motohiko Ezawa

Department of Applied Physics, University of Tokyo, Hongo 7-3-1, 113-8656, Japan

Borophene is a monolayer materials made of boron. A perfect planar borophene called β_{12} borophene has Dirac cones and they are well reproduced by a tight-binding model according to recent experimental and first-principles calculation results. We explicitly derive a Dirac theory for β_{12} borophene. Dirac cones are gapless when the inversion symmetry exists, while they are gapped when it is broken. In addition, three-band touching points emerge together with pseudospin triplet fermions when all transfer energy is equal and all on-site energy is equal. The three-band touching is slightly resolved otherwise. We construct effective three-band theories for triplet fermions. We also study the edge states of borophene nanoribbons, which show various behaviors depending on the way of edge terminations.

I. INTRODUCTION

Monolayer material science is one of the most active fields of condensed matter physics in this decade. It has begun with graphene¹ and been extended to the group IV monolayer materials² including silicene³⁻⁵, germanene⁶⁻⁸ and stanene⁹. Furthermore, experimental success of phosphorene¹⁰⁻¹² has opened a field of the group V monolayer materials including arsenene¹³ and antimonene¹⁴. A search for new monolayer materials is extended to the group III monolayer materials including borophene and aluminene¹⁵. Especially, several types of borophene are proposed by first-principles calculation¹⁷⁻²². Recently, several types of borophene is synthesized on Ag(111)²³⁻²⁶.

In particular, β_{12} borophene experimentally manufactured on the silver surface²⁷ is quite interesting. Dirac fermions are clearly observed by the ARPES experiments as well as by first-principles calculation. The band structure is well reproduced by a tight-binding model, where it is enough to take into account only the p_z orbitals due to its perfect planar structure. The unit cell contains five atoms as in Fig.1(a). The lattice has a perfectly flat structure as in Fig.1(b). It can be constructed by adding atoms indicated in yellow into the honeycomb lattice.

In this paper we study the band structure of β_{12} borophene based on the tight-binding model²⁷. In particular we explore the band touching problem at high-symmetry points. When we assume an identical transfer energy t_{ij} and an on-site energy ε_i , massless Dirac fermions emerge at two-band touching points (K and K' points), and different types of fermions emerge at three-band touching points (X , M , Λ and Λ' points). In particular, fermions at the X and M points constitute pseudospin triplets separately. Then we construct an effective two-band theory or three-band theory in the vicinity of each touching point. Next, we consider the models together with realistic parameters for t_{ij} and ε_i . We consider two models with and without the inversion symmetry by an appropriate choice of the on-site energies. We find anisotropic massive Dirac fermions with the use of inversion nonsymmetric parameters. The degeneracy at the three-band touching points are slightly resolved both for the inversion symmetric and nonsymmetric models. Finally we study the edge states of borophene nanoribbons.

This paper is composed as follows. In Sec. II we review the

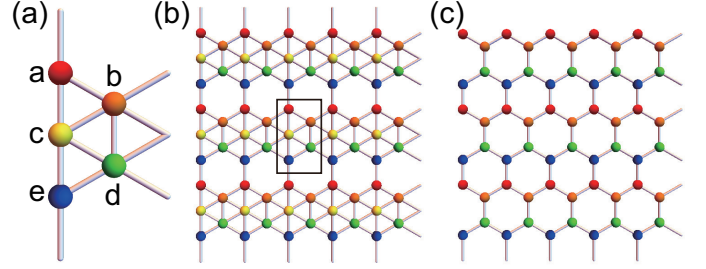


FIG. 1: (a) The unit cell of borophene, which contains five atoms. Each atoms are colored by red, orange, yellow, green and blue, which we label "a", "b", "c", "d" and "e" atoms, respectively. (b) The lattice structure of borophene. The unit cell is indicated by the black rectangle. (c) The honeycomb lattice obtained by removing the "c" atoms, which describes the effective four-band and two-band model.

basic properties of the lattice structure, the Brillouin zone and the symmetry for β_{12} borophene. In Sec. III, we start with a five-band model comprised of the p_z orbitals of Boron. We compare three types of models. One is a homogeneous model, where we take an identical transfer energy and an identical on-site energy. The second is the inversion symmetric model, where the transfer and on-site energies are chosen so as to respect the inversion symmetry. The third is the inversion non-symmetric model, where on-site energies breaks the inversion symmetry. We show that Dirac fermions are gapless (gapped) when the inversion symmetry is present (absent). In Sec.IV, we derive an effective Dirac theory for general parameters and confirm the above results. In Sec.V, we derive effective theories of fermions at three-band touching points. It is shown that the set of fermions at the X or M point is unitary equivalent to the triplet of the pseudospin ($J = \pm 1, 0$). In Sec.VI, we study edge states of borophene nanoribbons, where five different types of edges are introduced corresponding to the unit cell size.

II. β_{12} LATTICE

The lattice structure of β_{12} borophene is illustrated in Fig.1(b). The unit cell contains five atoms as in Fig.1(a). The "a" and "e" atoms have four bonds, the "b" and "d" atoms have five bonds, and the "c" atoms have six bonds, leading to

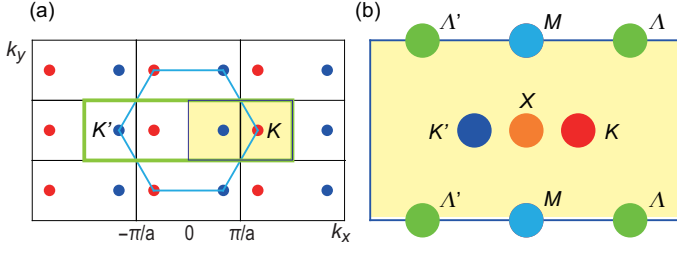


FIG. 2: (a) Brillouin zone of borophene indicated by the yellow rectangle with the blue boundary, and that of the honeycomb lattice indicated by a hexagon with the cyan boundary or equivalently a rectangle with the green boundary. The area of the former is one half of the latter. (b) Positions at which Dirac fermions (K, K') and triplet fermions (X, M) emerge in the Brillouin zone. Additionally there appear three-band touching points at Λ and Λ' .

different on-site potentials.

The Brillouin zone is a rectangle given by $-\pi/a \leq k_x \leq \pi/a$ and $-\pi/(\sqrt{3}a) \leq k_y \leq \pi/(\sqrt{3}a)$, as shown in Fig.2(a). However, it is convenient to use a shifted Brillouin zone $0 \leq k_x \leq 2\pi/a$ and $-\pi/(\sqrt{3}a) \leq k_y \leq \pi/(\sqrt{3}a)$. The area of the Brillouin zone of β_{12} borophene is one half of that of the honeycomb lattice. This is understood as follows. The β_{12} lattice without the "c" atoms is identical to the honeycomb lattice, where the unit cell contains four atoms. On the other hand, the honeycomb lattice has only two atoms in the unit cell. Namely, the Brillouin zone of the β_{12} borophene must be one half of that of the honeycomb lattice. There are four high-symmetry points in the Brillouin zone; K ($2\pi/3a, 0$), K' ($-2\pi/3a, 0$), X ($\pi/a, 0$) and M ($\pi/a, \pi/\sqrt{3}a$). Additionally there are two points; Λ ($\pi/3a, \pi/\sqrt{3}a$), Λ' ($-\pi/3a, \pi/\sqrt{3}a$). They play important roles in our analysis.

The symmetries of the lattice are the inversion symmetry I , the two mirror symmetries with respect to the x and y axes, M_x and M_y . There is a relation $I = M_x M_y$. On the other hand, the C_3 rotation symmetry present in the honeycomb lattice is absent in the β_{12} lattice.

III. FIVE-BAND MODEL

A recent first-principles calculation demonstrates that the system is well described only in terms of the p_z orbitals of the boron atoms²⁷, implying that the tight-binding model is five dimensional,

$$H_5 = \begin{pmatrix} \varepsilon_a & t_{ab}g & t_{ac}f^* & 0 & t_{ae}f \\ t_{ab}g^* & \varepsilon_b & t_{bc}g & t_{bd}f^* & 0 \\ t_{ac}f & t_{bc}g^* & \varepsilon_c & t_{cd}g & t_{ce}f^* \\ 0 & t_{bd}f & t_{cd}g^* & \varepsilon_d & t_{de}g \\ t_{ae}f^* & 0 & t_{ce}f & t_{de}g^* & \varepsilon_e \end{pmatrix} \quad (1)$$

with

$$f = e^{iak_y/\sqrt{3}}, \quad g = 2e^{-iak_y/2\sqrt{3}} \cos ak_x/2. \quad (2)$$

The parameters obtained by fitting first-principles calculation results are summarized as²⁷,

$$\begin{aligned} t_{ab} &= t_{de} = -2.04\text{eV}, & t_{ac} &= t_{ce} = -1.79\text{eV}, \\ t_{ae} &= -2.12\text{eV}, \\ t_{bc} &= t_{cd} = -1.84\text{eV}, & t_{bd} &= -1.91\text{eV}, \end{aligned} \quad (3)$$

showing that the transfer energies are symmetric along the x axis, and

$$\begin{aligned} \varepsilon_a &= \varepsilon_d = 0.196\text{eV}, & \varepsilon_b &= \varepsilon_e = -0.058\text{eV}, \\ \varepsilon_c &= -0.845\text{eV}. \end{aligned} \quad (4)$$

The lattice constant is $a = 2.9236\text{\AA}$. A characteristic feature is that the inversion symmetry of the lattice structure is broken by this set of on-site energies. The inversion symmetry breaking will be due to effects of the Ag substrate. We refer to this tight-binding model as the inversion nonsymmetric model.

We first consider the model²⁷ by setting all transfer energy equal ($t_{ij} = t = -2\text{eV}$) and all on-site energy zero ($\varepsilon_i = 0$), which we refer to as the homogeneous model. We also investigate the inversion symmetric model, which is defined by the following set of the one-site energies instead of (4),

$$\begin{aligned} \varepsilon_a &= \varepsilon_e = 0.196\text{eV}, & \varepsilon_b &= \varepsilon_d = -0.058\text{eV}, \\ \varepsilon_c &= -0.845\text{eV}, \end{aligned} \quad (5)$$

where the magnitude of the on-site energy reflects the number of adjacent atoms in each sites. We show the band structures of the homogeneous model and the inversion nonsymmetric model in Fig.3(a1) and Fig.3(b1), respectively. We also show their project band structures along the k_x axis in Fig.3(a2) and Fig.3(b2). Those for the inversion symmetric model are quite similar to these.

We start with the investigation of the homogeneous model: See Fig.3(a1). We find Dirac fermions at the K and K' points given by $\mathbf{K}_{\pm} = (\pm 2\pi/3a, 0)$, where the energy is explicitly calculated as

$$U_1^{-1} H_5(\mathbf{K}_{\pm}) U_1 = t \text{diag.} (0, 0, 1 \pm \sqrt{5}, -2) \quad (6)$$

with the use of a unitary transformation U_1 . It is interesting that there are different types of three-band touching points. Their positions in the Brillouin zone are shown in Fig.2(b). One is at the X point given by $\mathbf{X} = (\pi/a, 0)$, where the energy is

$$U_2^{-1} H_5(\mathbf{X}) U_2 = t \text{diag.} (-1, -1, -1, 1, 2). \quad (7)$$

The second one is at the M point given by $\mathbf{M} = (\pi/a, \pi/\sqrt{3}a)$, where the energy is

$$U_3^{-1} H_5(\mathbf{M}) U_3 = t \text{diag.} (1, 1, 1, -1, -2). \quad (8)$$

The third one is at the Λ and Λ' points given by $\mathbf{\Lambda}_{\pm} = (\pm\pi/3a, \pi/\sqrt{3}a)$, where the energy is

$$U_4^{-1} H_5(\mathbf{\Lambda}_{\pm}) U_4 = t \text{diag.} (-2, -2, -2, 2, 4). \quad (9)$$

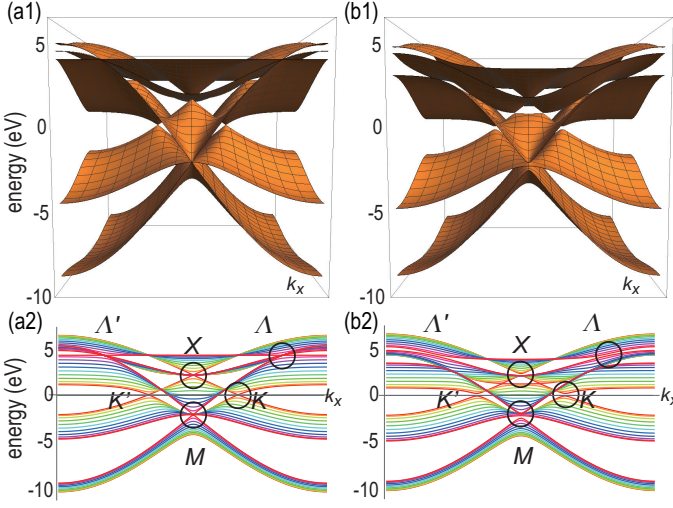


FIG. 3: Bird's eye's views of the band structure of (a1) the homogeneous model and (b1) the inversion nonsymmetric model. The projected band structure along the k_x direction of (a2) the homogeneous model and (b2) the inversion nonsymmetric model. Gapless Dirac fermions (K, K') and gapless triplet fermions (X, M) emerge in the homogeneous model. In the inversion nonsymmetric model, Dirac fermions have a tiny gap (~ 0.254 eV), while the degeneracy of triplet fermions is slightly resolved.

We show the detailed band structures of Dirac fermions and triple-point fermions in Fig.4(a1),(b1),(c1) and (d1).

We may investigate both the inversion symmetric and nonsymmetric models in a similar way. Their overall band structures are very similar to that of the homogeneous model, as shown in Fig.3(b1) for the inversion nonsymmetric model. However, there arise differences with respect to the degeneracy at the band touching points. First, the Dirac fermions remain gapless in the inversion symmetric model but gets gapped in the inversion nonsymmetric model. On the other hand, three-band touching points are slightly resolved both in the inversion symmetric and nonsymmetric models. We show the detailed band structure at these points in Fig.4.

IV. DIRAC FERMIONS

Since the dimension of the matrix in the tight-binding model (1) is five, it is impossible to diagonalize it analytically. It is highly desirable to construct such models with lower dimensions that we can analyze analytically. We construct an effective two-band Hamiltonian for Dirac fermions in this section and effective three-band Hamiltonians for fermions at three-band touching points in the next section.

It is reported²⁷ that the amplitude of the zero-energy wave function at the K and K' points is exactly zero at the "c" sites for the homogeneous model. Then, it is reasonable to neglect the "c" atoms in the Hamiltonian (1), and we obtain the following four-band Hamiltonian to describe the physics

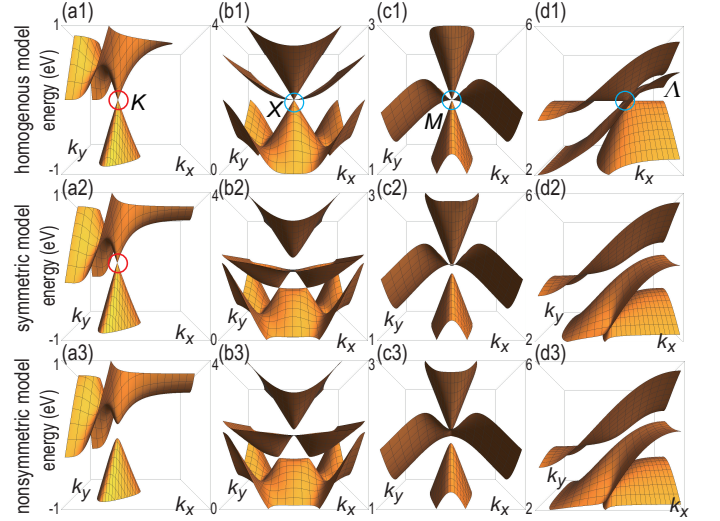


FIG. 4: Band structures in the vicinity of the Dirac point (K) indicated by a magenta circle and the three-band touching points (X, M, Λ) indicated by cyan circles: (a1)~(d1) for the homogeneous model; (a2)~(d2) for the inversion symmetric model; (a3)~(d3) for the inversion nonsymmetric model. Dirac fermions remain gapless while the three-band touching are slightly resolved in the inversion symmetric model. Dirac fermions become gapped in the inversion nonsymmetric model.

in the vicinity of the K and K' points,

$$H_5 = \begin{pmatrix} 0 & g & 0 & f \\ g^* & 0 & f^* & 0 \\ 0 & f & 0 & g \\ f^* & 0 & g^* & 0 \end{pmatrix}. \quad (10)$$

The energy is analytically obtained as

$$E = \pm \sqrt{f - g} \sqrt{f^* - g^*}, \pm \sqrt{f + g} \sqrt{f^* + g^*} \\ = \pm t \sqrt{3 + 2 \cos ak_x \pm 2 \sqrt{(1 + \cos ak_x) (1 + \cos \sqrt{3} ak_y)}}. \quad (11)$$

Indeed, as we show in Fig.5(a), it well reproduces the original band structure of the Dirac fermions both at the K and K' points.

The corresponding lattice is a honeycomb lattice shown in Fig.1(c). The unit cell contains four atoms comprised of the "a", "b", "d" and "e" atoms. On the other hand, the unit cell of the honeycomb lattice contains two atoms such as "b" and "d". Hence the above four-band model can be further reduced to the two-band model.

We are able to construct actually the two-band model by way of $H_2(\mathbf{k}) = P_2 U_1^{-1} H_5(\mathbf{k}) U_1 P_2$ in the vicinity of the K and K' points, where P_2 is the projection operator from the 5×5 Hamiltonian to the 2×2 Hamiltonian containing the two bands with the zero eigen-energy. The low-energy effective Hamiltonian at the K point is given by

$$H_2 = \begin{pmatrix} (\varepsilon_b + \varepsilon_e)/2 & F \\ F^* & (\varepsilon_a + \varepsilon_d)/2 \end{pmatrix} \quad (12)$$

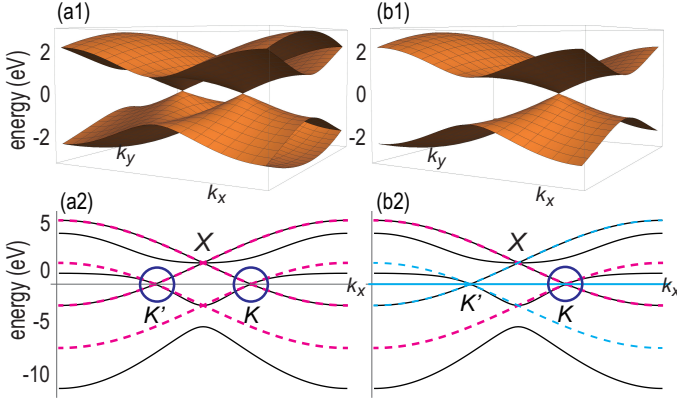


FIG. 5: Bird's eye's views of the band structure of (a1) the effective four-band model and (b1) the effective two-band model for the K point. The band structure along the k_x direction at $k_y = 0$ for (a2) the effective four-band model (in magenta), (b2) the effective two-band models at the K point (in magenta) and at the K' point (in cyan), together with the band structure of the five-band model (in black).

with

$$F = \frac{t_{ae} + t_{bd}}{2} e^{-iak_y/\sqrt{3}} + (t_{ab} + t_{de}) e^{iak_y/2\sqrt{3}} \cos \frac{ak_x}{2}. \quad (13)$$

It is identical to the Hamiltonian of the anisotropic honeycomb lattice with on-site potentials,²⁸ which corresponds to the lattice without the "c" atoms. This correspondence is due to the fact that the amplitude of the wave function at the "c" sites is zero at the zero energy. We show a bird's eye's view of the band structure in Fig.5(b1).

The gap closes at

$$\tilde{K} = \left(\frac{2}{a} \arccos \frac{-(t_{ae} + t_{bd})}{2(t_{ab} + t_{de})}, 0 \right), \quad (14)$$

when $\varepsilon_a - \varepsilon_b + \varepsilon_d - \varepsilon_e = 0$. Especially, the gap closes in the presence of the inversion symmetry since $\varepsilon_a = \varepsilon_e$ and $\varepsilon_b = \varepsilon_d$. The gap closing point shifts from the original K point when $t_{ae} + t_{bd} \neq t_{ab} + t_{de}$. The gap opens when $\varepsilon_a - \varepsilon_b + \varepsilon_d - \varepsilon_e \neq 0$ with the gap $|\varepsilon_a - \varepsilon_b + \varepsilon_d - \varepsilon_e|/2$. We estimate the gap is 0.254eV by using the parameters (4) in the inversion nonsymmetric model.

We show the band structure along the k_x axis of the two-band model as well as the five-band model in Fig.5(b2) in magenta and black, respectively. The Dirac fermions at the K point is well reproduced, while the Dirac fermions at the K' point disappear. This is due to the fact that the Brillouin zone is enlarged twice since the unit cell becomes half compared with that of the four-band model, as shown in Fig.2. We may construct another two-band model at the K' point precisely in the similar way, whose result we also present in Fig.5(b2) in cyan. The combination of the two-band models at the K and K' points perfectly reproduces the four-band model.

In the vicinity of the K point, the two-band Hamiltonian is

expanded as

$$H_2^K = -\frac{\varepsilon_a - \varepsilon_b + \varepsilon_d - \varepsilon_e}{4} \tau_z - \frac{\varepsilon_a - \varepsilon_b + \varepsilon_d - \varepsilon_e}{4} \tau_0 - \frac{\sqrt{4(t_{ab} + t_{de})^2 - (t_{ae} + t_{bd})^2}}{4} a (k_x - \tilde{K}) \tau_x + \frac{\sqrt{3}}{4} (t_{ae} + t_{bd}) ak_y \tau_y, \quad (15)$$

which represents a Dirac cone. Here we have introduced the unit matrix τ_0 and the Pauli matrix $\tau = (\tau_x, \tau_y, \tau_z)$ for the pseudospin degrees of freedom describing the two bands. The dispersion is isotropic only for the homogeneous model.

In passing, it is intriguing to see that the four-band theory reproduces precisely two bands at the X point though it is constructed solely for the K and K' points in Fig.5.

V. FERMIONS AT THREE-BAND TOUCHING POINTS

We next construct three-band effective models for fermions at three-band touching points. We construct effective models as in the case of the Dirac fermions with the use of the unitary transformation and the projection to the low-energy bands.

X point: The effective Hamiltonian valid in the vicinity of the X point is given by

$$H_3^X = t \begin{pmatrix} F_{aa}^X & F_{ab}^X & F_{ac}^X \\ F_{ab}^{X*} & F_{bb}^X & F_{bc}^X \\ F_{ac}^{X*} & F_{bc}^{X*} & F_{cc}^X \end{pmatrix}, \quad (16)$$

where

$$\begin{aligned} F_{aa}^X &= F_{bb}^X = F_{cc}^X = -\cos \frac{ak_y}{\sqrt{3}}, \\ F_{ab}^X &= 2 \cos \frac{ak_x}{2} \cos \frac{ak_y}{2\sqrt{3}}, \quad F_{ac}^X = i\sqrt{3} \sin \frac{ak_y}{\sqrt{3}}, \\ F_{bc}^X &= 2i\sqrt{3} \cos \frac{ak_x}{2} \sin \frac{ak_y}{2\sqrt{3}} \end{aligned} \quad (17)$$

in the case of the homogeneous model. See Appendix for general parameters.

We show the band structure in Fig.6(a1). The vicinity of the three-band touching point is well reproduced by this model. Furthermore, comparing the band structure of the three-band model H_3^X along the $k_y = 0$ line with that of the original five-band model H_5 , the three-band model H_3^X is found to reproduce perfectly the two bands given by $E = \pm 2 \cos(ak_x/2) - 1$ all over the region: See 6(a2).

We wonder why there is no partner for the X point as in the case of the K and K' points. We study this problem for the homogeneous model. The three-band Hamiltonian is expanded in the vicinity of the X point as

$$H_3^X = -t + ta \begin{pmatrix} 0 & -k'_x & ik_y \\ -k'_x & 0 & 0 \\ -ik_y & 0 & 0 \end{pmatrix} \quad (18)$$

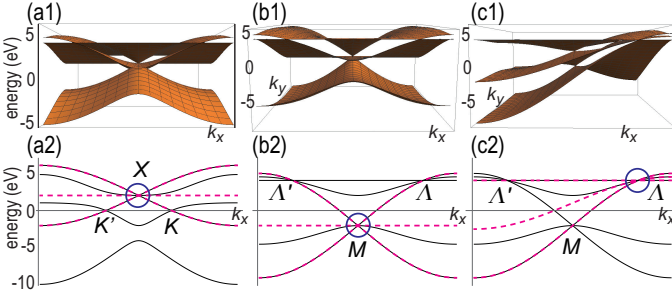


FIG. 6: Bird's eye's views of the band structure of the effective three-band models describing fermions at (a1) the X point, (b1) the M point and (c1) the Λ point. (a2)~(c2) Black curves represent the band structure of the five-band model (1) along the k_x axis. Magenta curves represent that of (a2) the two-band model (12) at the X point ($k_y = 0$), (b2) the three-band model (16) at the M point ($k_y = \pi/(\sqrt{3}a)$), and (c2) the three-band model (23) at the Λ point ($k_y = \pi/(\sqrt{3}a)$).

with $k'_x = k_x \mp \frac{\pi}{a}$. The corresponding wave functions are

$$\psi_0 = \{0, i \sin \theta, \cos \theta\}^t, \quad (19)$$

$$\psi_{\pm} = \frac{1}{\sqrt{2}} \{\pm i, -i \cos \theta, \sin \theta\}^t. \quad (20)$$

The Berry phase is zero for each band,

$$\Gamma_B = -i \int d\theta \langle \psi_0 | \frac{\partial}{\partial \theta} | \psi_0 \rangle = -i \int d\theta \langle \psi_{\pm} | \frac{\partial}{\partial \theta} | \psi_{\pm} \rangle = 0. \quad (21)$$

Since the band carries no topological charge, the X point can exist by itself. Furthermore, it indicates that the three-band touching point is not topologically protected.

The energy eigenstate of the Hamiltonian (18) is given by $E = -t, -t \pm \sqrt{k_x'^2 + k_y'^2}$. Hence it is unitary equivalent to the following Hamiltonian,

$$H = -t + ta(k'_x J_x + k_y J_y), \quad (22)$$

where $\mathbf{J} = (J_x, J_y, J_z)$ is the pseudospin operator obeying $[J_x, J_y] = J_z$, etc., whose magnitude is $J = 1$. Namely, the three bands are members of a pseudospin triplet with $J = \pm 1, 0$. On the other hand, for realistic t_{ij} and ε_i , the three-band touching point is slightly resolved.

M point: In the vicinity of the M point, we obtain the following effective three-band model,

$$H_3^M = t \begin{pmatrix} F_{aa}^M & F_{ab}^M & F_{ac}^M \\ F_{ab}^{M*} & F_{bb}^M & F_{bc}^M \\ F_{ac}^{M*} & F_{bc}^{M*} & F_{cc}^M \end{pmatrix}, \quad (23)$$

where

$$\begin{aligned} F_{aa}^M &= F_{bb}^M = F_{cc}^M = \frac{1}{2} \left(\cos \frac{ak_y}{\sqrt{3}} + \sqrt{3} \sin \frac{ak_y}{\sqrt{3}} \right), \\ F_{ab}^M &= (-1)^{2/3} \cos \frac{ak_x}{2} \left(\sqrt{3} \sin \frac{ak_y}{2\sqrt{3}} - \cos \frac{ak_y}{2\sqrt{3}} \right), \\ F_{ac}^M &= \frac{\sqrt{3}}{2} (-1)^{5/6} \left(\sin \frac{ak_y}{\sqrt{3}} - \sqrt{3} \cos \frac{ak_y}{\sqrt{3}} \right), \\ F_{bc}^M &= (-1)^{1/6} \sqrt{3} \cos \frac{ak_x}{2} \left(\sin \frac{ak_y}{2\sqrt{3}} + \sqrt{3} \cos \frac{ak_y}{2\sqrt{3}} \right) \end{aligned} \quad (24)$$

in the case of the homogeneous model. See Appendix for general parameters.

We show the band structure in Fig.6(b1). In Fig.6(b2), comparing the band structure of the three-band model H_3^M along the $k_y = \pi/\sqrt{3}a$ line with that of the five-band model H_5 , we find that the three-band model H_3^M perfectly reproduces the two-bands given by $E = t \pm 2 \cos \frac{ak_x}{2}$ all over the region. On the other hand, the middle band becomes a perfect flat band in the three-band model H_3^M , while it is dispersive in the five-band model H_5 .

We expand the three-band Hamiltonian in the vicinity of the M point as

$$H_3^M = t + ta \begin{pmatrix} 0 & 0 & e^{5i\pi/6} k'_y \\ 0 & 0 & -\sqrt{3} e^{i\pi/6} k'_x \\ e^{-5i\pi/6} k'_y & -\sqrt{3} e^{-i\pi/6} k'_x & 0 \end{pmatrix} \quad (25)$$

with $k'_x = k_x - \pi/a$, $k'_y = k_y - \pi/\sqrt{3}a$. The energy is obtained as $E = t, t \pm \sqrt{3k_x'^2 + k_y'^2}$. Hence it is unitary equivalent to the following Hamiltonian,

$$H = t + ta(\sqrt{3}k'_x J_x + k_y J_y). \quad (26)$$

The three bands are members of a pseudospin triplet with $J = \pm 1, 0$. The Berry phase is zero for each band. Consequently, the M point is not accompanied by a partner. These properties are quite similar to those of the X point.

Λ point: In the vicinity of the Λ point, we obtain the following effective three-band model,

$$H_3^{\Lambda} = t \begin{pmatrix} F_{aa}^{\Lambda} & F_{ab}^{\Lambda} & F_{ac}^{\Lambda} \\ F_{ab}^{\Lambda*} & F_{bb}^{\Lambda} & F_{bc}^{\Lambda} \\ F_{ac}^{\Lambda*} & F_{bc}^{\Lambda*} & F_{cc}^{\Lambda} \end{pmatrix} \quad (27)$$

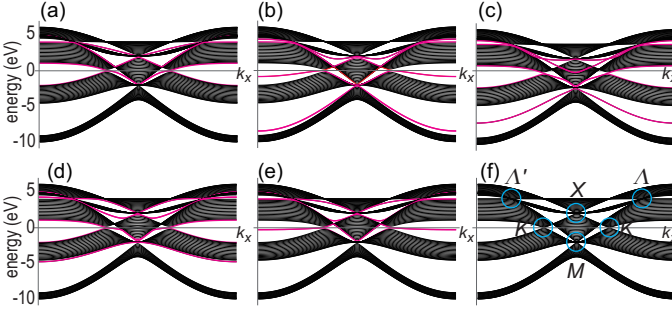


FIG. 7: Band structures of zigzag borophene nanoribbon. (a) The upper edge is terminated by "a" atoms, while the lower edge is terminated by "e" atoms. (b) The upper edge is terminated by "b" atoms, while the lower edge is terminated by "d" atoms. (c) Both edges are terminated by "c" atoms. (d) The upper edge is terminated by "d" atoms, while the lower edge is terminated by "b" atoms. (e) The upper edge is terminated by "e" atoms, while the lower edge is terminated by "a" atoms. One edge state connects a Dirac point and a triple point. The edge states are colored in magenta. (f) The projected band structure of the bulk along the k_x axis, which is the same one as Fig.3(a2).

with

$$\begin{aligned}
 F_{aa}^\Lambda &= F_{bb}^\Lambda = F_{cc}^\Lambda = -\frac{1}{4} \left[\cos \frac{ak_y}{\sqrt{3}} + \sqrt{3} \sin \frac{ak_y}{\sqrt{3}} \right. \\
 &\quad \left. + 2\sqrt{3} \cos \frac{ak_x}{2} \left(\sqrt{3} \cos \frac{ak_y}{2\sqrt{3}} + \sin \frac{ak_y}{2\sqrt{3}} \right) \right], \\
 F_{ab}^\Lambda &= \frac{1}{4} (-1)^{2/3} \left[-3 \cos \frac{ak_y}{\sqrt{3}} + \sqrt{3} \sin \frac{ak_y}{\sqrt{3}} \right. \\
 &\quad \left. + 2 \cos \frac{ak_x}{2} \left(\sqrt{3} \sin \frac{ak_y}{2\sqrt{3}} - \cos \frac{ak_y}{2\sqrt{3}} \right) \right], \\
 F_{ac}^\Lambda &= \frac{\sqrt{3}}{2} e^{-iak_y/\sqrt{3}} (-1)^{2/3} + \frac{\sqrt{3}}{4} e^{iak_y/\sqrt{3}} \\
 &\quad - \frac{3i}{2} e^{-iak_y/2\sqrt{3}} \cos \frac{ak_x}{2}, \\
 F_{bc}^\Lambda &= \left[\frac{\sqrt{3}}{2} (-1)^{1/6} e^{-iak_y/2\sqrt{3}} + \sqrt{3} e^{iak_y/2\sqrt{3}} \right] \cos \frac{ak_x}{2} \\
 &\quad + \frac{3}{4} (-1)^{1/6} e^{iak_y/\sqrt{3}}. \tag{28}
 \end{aligned}$$

We show the band structure in Fig.6(c1). In Fig.6(c2), we compare the band structure of the three-band model H_3^C along the $k_y = \pi/\sqrt{3}a$ line with that of the original five-band model H_5 , and find that the three band model H_3^C perfectly reproduces the two bands given by $E = -2t, t - 2 \cos \frac{ak_x}{2}$ all over the region.

In the vicinity of the Λ point, the Hamiltonian is expanded as

$$H_3^\Lambda = -2t + \frac{\sqrt{3}}{4} ak_x + \frac{ta}{4} \begin{pmatrix} 0 & F_{ab}^{C'} & F_{ac}^{C'} \\ F_{ab}^{C'*} & 0 & F_{bc}^{C'} \\ F_{ac}^{C'*} & F_{bc}^{C'*} & 0 \end{pmatrix} \tag{29}$$

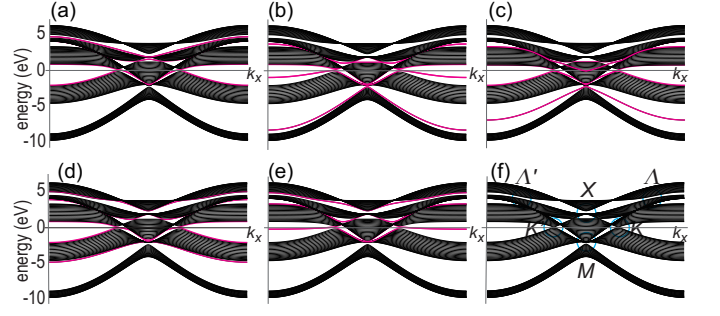


FIG. 8: Band structures of zigzag borophene nanoribbon with inversion symmetric parameters. The edge states are almost identical to the case for the homogeneous parameters although three-band touchings are slightly resolved at the X , M , Λ and Λ' points. These results show that edge states are robust for the choice of the parameters. See also the caption of Fig.7.

with

$$\begin{aligned}
 F_{ab}^{C'} &= 3(-1)^{2/3} k_y \\
 F_{ac}^{C'} &= \frac{1}{2} (-1)^{1/3} (3k_x + ik_y) \\
 F_{bc}^{C'} &= -\frac{\sqrt{3}}{2} (-1)^{1/6} k_- \tag{30}
 \end{aligned}$$

and $k'_x = k_x - \pi/(3a)$, $k'_y = k_y - \pi/(\sqrt{3}a)$.

Although the Λ and Λ' points appear in a pair, we are unable so far to reveal the reason. Indeed, we are unable to assign topological charges to them, because the triple band touching at the Λ point is highly tilted as in Fig.6(c1) and the Fermi surface is no longer a point. Accordingly there is no loop encircling the triple band touching point without touching the Fermi surface, as disables us to calculate the Berry phase.

VI. BOROPHENE NANORIBBONS

When a nanoribbons is along the zigzag direction there are zigzag and beard edges in the case of the honeycomb system. This is because there are two atoms in the unit cell. There are five types of borophene nanoribbons with zigzag edges corresponding to the fact that the unit cell contains five atoms. For example, the edge terminated by "a","b", "c" and "d" atoms forms a zigzag edge, while that terminated by "e" atoms forms a beard edge on one side. Thus there are $5 \times 5 = 25$ different nanoribbons.

We show the band structure of typical nanoribbons in Fig.7(a)~(e). In Fig.7(f), we show the bulk band structure projected to the k_x axes for the sake of comparison. The band structure of nanoribbons are almost identical to those of the projected bulk band structure except for the edge states, which are marked by magenta curves. The edge states emerge in the region connecting between the Dirac point and the triple point. Among them, there emerge almost flat bands at the zero energy in Fig.7(e), which corresponds to the beard edge states. If the two terminations are different, the edge states are the sum of the two terminations.

We also show the band structure of borophene nanoribbons with the use of the inversion symmetric parameters in Fig.8. Edge states remain as it is although the band touchings are resolved at the three-band touching points. These results show that edge states are robust for the choice of model parameters.

VII. DISCUSSION

It is interesting that Dirac fermions and triplet fermions emerge at the high-symmetry points in the β_{12} structure of borophene. There is a distinctive difference between them. On one hand, Dirac fermions emerge always in a pair: They emerge at the K and K' points just as in graphene. The reason is the Nielsen-Ninomiya theorem. Namely, the gapless Dirac fermion has $\pm\pi$ Berry phase while the gapped Dirac fermion has $\pm 1/2$ Chern number. They appear in a pair so that the total topological number is zero.

On the other hand, this is not the case for triplet fermions. There are no partners for the X and M points. Indeed, calculating the Berry phases of the bands at X and M , we find them to be zero. With respect to the Λ and Λ' points, although they appear in a pair, we are unable to reveal the reason, because we are unable to assign topological charges to them.

We have considered the homogeneous, inversion symmetric and nonsymmetric models. All of the three models are not applicable to borophene on the Ag substrate due to the incommensurability of the lattices. Furthermore, the β_{12} structure itself already induces some inhomogeneity: there are four-fold (a,e), five-fold (b,d) and six-fold (c) coordinated atoms, as in Fig.1. Nevertheless, it is important to study free-standing borophene although it has not yet been manufactured. Among them, the homogeneous model provides us with a basic and clear understanding of the electronic properties of borophene.

The lattice structure of β_{12} borophene has the inversion symmetry, where massless Dirac fermions are expected. However, the inversion symmetry is broken in the Hamiltonian together with the parameters (3) presented in Ref.²⁷, where Dirac fermions are gapped. Our results show that there exists a gap (0.254eV) with the use of the inversion nonsymmetric parameters. On the other hand, the ARPES experiment and first-principles calculations show that the gap is absent within the experimental resolution. The inconsistency between

the inversion nonsymmetric model and the ARPES experiment will be due to the incommensurability of the Ag and borophene lattices, which breaks the symmetry given by (4). It seems that the inversion symmetric model is most natural among the three models studied in this paper.

We note that there is a metallic band at the zero-energy in the five-band model, while it is absent in the effective lower-band theories. This is because that they are valid only in the vicinity of the high-symmetry points. We should use the five-band model when we calculate the conductivity and others.

We have so far ignored the spin-orbit interactions because they are expected to be small in the absence of the substrate due to the following reasons. One is that boron is a light element which is comparable to carbon. Spin-orbit interactions are tiny in materials consisting of light elements. For example, it is well known that graphene has tiny spin-orbit interactions. In addition, phosphorene is also known to have negligible spin-orbit interactions. Another reason is that planar monolayer materials have tiny spin-orbit interactions such as graphene since the inversion symmetry is not broken. For example, the Kane-Mele interaction is negligible for the planar honeycomb system, although it is significant for buckled honeycomb system such as silicene, germanene and stanene. Furthermore, the Rashba interaction is also zero in the absence of the perpendicular electric field since it requires inversion symmetry breaking. On the other hand, there is a possibility that the substrate induces the Rashba interaction as in the case of graphene on the substrate, where the Rashba spin-orbit interaction is introduced by the inversion symmetry breaking due to the substrate²⁹.

The author is very much grateful to N. Nagaosa for many helpful discussions on the subject. He thanks the support by the Grants-in-Aid for Scientific Research from MEXT KAKENHI (Grant Nos. JP17K05490, JP25400317 and JP15H05854). This work is also supported by JST, CREST (Grant No. JPMJCR16F1).

Appendix: Three-band theories with general parameters

In this appendix we present the matrix elements of the effective three-band theories (16) for the X point and (23) for the M point with general parameters t_{ij} and ε_i .

For the X point we obtain

$$\begin{aligned}
F_{aa}^X &= \frac{\varepsilon_a + \varepsilon_e}{2} - t_{ae} \cos \frac{ak_y}{\sqrt{3}}, \\
F_{bb}^X &= \frac{\varepsilon_b + \varepsilon_d}{2} - t_{bd} \cos \frac{ak_y}{\sqrt{3}}, \\
F_{cc}^X &= \frac{\varepsilon_a + 4\varepsilon_c + \varepsilon_e}{6} - \frac{2t_{ac} - t_{ae} + 2t_{ce}}{3} \cos \frac{ak_y}{\sqrt{3}}, \\
F_{ab}^X &= \left(t_{ab} e^{-\frac{iak_y}{2\sqrt{3}}} + t_{cd} e^{\frac{iak_y}{2\sqrt{3}}} \right) \cos \frac{ak_x}{2}, \\
F_{ac}^X &= \frac{\varepsilon_a - \varepsilon_e}{2\sqrt{3}} + \frac{-t_{ac} + t_{ce}}{\sqrt{3}} \cos \frac{ak_y}{\sqrt{3}} + i \frac{t_{ac} + t_{ae} + t_{ce}}{\sqrt{3}} \sin \frac{ak_y}{\sqrt{3}}, \\
F_{bc}^X &= \frac{-(t_{de} + 2t_{bc}) e^{-\frac{iak_y}{2\sqrt{3}}} + (t_{ab} + 2t_{cd}) e^{\frac{iak_y}{2\sqrt{3}}}}{\sqrt{3}} \cos \frac{ak_x}{2}.
\end{aligned} \tag{31}$$

For M point we obtain

$$\begin{aligned}
F_{aa}^M &= \frac{\varepsilon_a + \varepsilon_e}{2} + \frac{t_{ae}}{2} \cos \frac{ak_y}{\sqrt{3}} + \sqrt{3} t_{ae} \sin \frac{ak_y}{\sqrt{3}}, \\
F_{bb}^M &= \frac{\varepsilon_b + \varepsilon_d}{2} + \frac{t_{bd}}{2} \cos \frac{ak_y}{\sqrt{3}} + \sqrt{3} t_{bd} \sin \frac{ak_y}{\sqrt{3}}, \\
F_{cc}^M &= \frac{\varepsilon_a + 4\varepsilon_c + \varepsilon_e}{6} + \frac{2t_{ac} - t_{ae} + 2t_{ce}}{6} \left(\cos \frac{ak_y}{\sqrt{3}} + \sqrt{3} \sin \frac{ak_y}{\sqrt{3}} \right), \\
F_{ab}^M &= \left(\frac{e^{-2i\pi/3}}{4} t_{ab} e^{i\frac{ak_y}{2\sqrt{3}}} + t_{de} e^{-i\frac{ak_y}{2\sqrt{3}}} \right) \cos \frac{k_x}{2}, \\
F_{ab}^M &= \frac{e^{-i\pi/3} (2t_{ac} - t_{ae}) e^{-i\frac{ak_y}{\sqrt{3}}} + (t_{ae} + t_{ce}) e^{-i\frac{ak_y}{\sqrt{3}}} + \frac{-e^{i\pi/3} (\varepsilon_a - \varepsilon_e)}{2\sqrt{3}}}{2\sqrt{3}}, \\
F_{bc}^M &= \left((t_{ab} + 2t_{cd}) e^{-i\frac{ak_y}{2\sqrt{3}}} + \frac{(-1)^{1/3}}{\sqrt{3}} (t_{bc} + 2t_{de}) e^{i\frac{ak_y}{2\sqrt{3}}} \right) \cos \frac{ak_x}{2}.
\end{aligned} \tag{32}$$

-
- ¹ A.H. Castro Neto, F. Guinea, N.M.R. Peres, K.S. Novoselov, and A.K. Geim, *Rev. Mod. Phys.* **81**, 109 (2009).
 - ² M. Ezawa, *J. Phys. Soc. Jpn.* **84**, 121003 (2015).
 - ³ C.-C. Liu, H. Jiang, and Y. Yao, *Phys. Rev. B* **84**, 195430 (2011).
 - ⁴ M. Ezawa, *Phys. Rev. Lett.* **109**, 055502 (2012).
 - ⁵ L. Tao, E. Cinquanta, D. Chiappe, C. Grazianetti, M. Fanciulli, M. Dubey, A. Molle, and D. Akinwande, *Nature Nanotechnology* **10**, 227 (2015).
 - ⁶ M. E. Davila, L. Xian, S. Cahangirov, A. Rubio, G. Le Lay, *New J. Phys.* **16**, 095002 (2014).
 - ⁷ L. Li, S.-Z. Lu, J. Pan, Z. Qin, Y.-Q. Wang, Y. Wang, G.-Y. Cao, S. Du, and H.-J. Gao, *Adv. Mater.* **26**, 4820 (2014).
 - ⁸ M. Derivaz, D. Dentel, R. Stephan, M.-C. Hanf, A. Mehdaoui, P. Sonnet, and C. Pirri, *Nano Lett.* **15**, 2510 (2015).
 - ⁹ F. Zhu, W. Chen, Y. Xu, C. Gao, D. Guan, C. Liu, D. Qian, S.-C. Zhang, and J. Jia, *Nat. Mater.* **14**, 1020 (2015).
 - ¹⁰ L. Li, Y. Yu, G. J. Ye, Q. Ge, X. Ou, H. Wu, D. Feng, X. H. Chen, and Y. Zhang, *Nat. Nanotech.* **9** 372 (2014).
 - ¹¹ H. Liu, A. T. Neal, Z. Zhu, Z. Luo, X. Xu, D. Tomanek, and P. D. Ye, *ACS Nano* **8**, 4033 (2014).
 - ¹² F. Xia, H. Wang, and Y. Jia, *Nat. Com.* **5**, 4458 (2014).
 - ¹³ C. Kamal and M. Ezawa, *Phys. Rev. B* **91**, 085423 (2015).
 - ¹⁴ S. Zhang, Z. Yan, Y. Li, Z. Chen, and H. Zeng, *Ange. Chem.* **54**, 3112 (2015).
 - ¹⁵ C. Kamal, A. Chakrabarti and M. Ezawa, *New J. Phys.* **17**, 083014 (2015).
 - ¹⁶ M.H. Evans, J. D. Joannopoulos, and S. T. Pantelides, *Phys. Rev. B* **72**, 045434 (2005).
 - ¹⁷ H. Tang and S. Ismail-Beigi, *Phys. Rev. B* **82**, 115412 (2010); H. Tang and S. Ismail-Beigi, *Phys. Rev. Lett.* **99**, 115501 (2007).
 - ¹⁸ X. Wu, J. Dai, Y. Zhao, Z. Zhuo, J. Yang, and X. C. Zeng, *ACS Nano* **6**, 7443 (2012).
 - ¹⁹ E.S. Penev, S. Bhowmick, A. Sadrzadeh, and B. I. Yakobson, *Nano Lett.* **12**, 2441 (2012).
 - ²⁰ H. Liu, J. Gao, and J. Zhao, *Sci. Rep.* **3**, 3238 (2013).
 - ²¹ Y. Liu, E. S. Penev, and B. I. Yakobson, *Angew. Chem., Int. Ed.* **52**, 3156 (2013).
 - ²² Z. Zhang, Y. Yang, G. Guo, and B. I. Yakobson, *Angew. Chem. Int. Ed.* **54**, 13022 (2015).
 - ²³ A.J. Mannix, X.-F. Zhou, B. Kiraly, J. D. Wood, D. Alducin, B. D.

- Myers, X. Liu, B. L. Fisher, U. Santiago, J.R. Guest, M. J. Yacaman, A. Ponce, A.R. Oganov, M.C. Hersam, and N. P. Guisinger, *Science* 350, 1513 (2015).
- ²⁴ Z. Zhang, E. S. Penev, and B. I. Yakobson, *Nat. Chem.* 8, 525 (2016).
- ²⁵ B. Feng, J. Zhang, Q. Zhong, W. Li, S. Li, H. Li, P. Cheng, S. Meng, L. Chen, and K. Wu, *Nat. Chem.* 8, 563 (2016).
- ²⁶ B. Feng, J. Zhang, R.-Y. Liu, T. Iimori, C. Lian, H. Li, L. Chen, K. Wu, S. Meng, F. Komori, and I. Matsuda, *Phys. Rev. B* 94, 041408(R) (2016).
- ²⁷ B. Feng, O. Sugino, R.-Y. Liu, J. Zhang, R. Yukawa, M. Kawamura, T. Iimori, H. Kim, Y. Hasegawa, H. Li, L. Chen, K. Wu, H. Kumigashira, F. Komori, T.-C. Chiang, S. Meng, and I. Matsuda, *Phys. Rev. Lett.* 118, 096401 (2017).
- ²⁸ M. Ezawa, *New J. Phys.* 16, 115004 (2014).
- ²⁹ Z. Wang, D. K. Ki, H. Chen, H. Berger, A. H. MacDonald and A. F. Morpurgo, *Nat. Com.* 6, 8339 (2015).